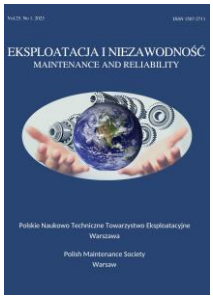

Eksploatacja i Niezawodnosc – Maintenance and Reliability

Volume 25 (2023), Issue 1

journal homepage: http://www.ein.org.pl

Article citation info:
Kłosowski G, Rymarczyk T, Niderla K, Kulisz M, Skowron Ł, Soleimani M. Using an LSTM network to monitor industrial reactors using electrical capacitance and impedance tomography – a hybrid approach. Eksploatacja i Niezawodnosc – Maintenance and Reliability 2023: 25(1) http://doi.org/10.17531/ein.2023.1.11

Using an LSTM network to monitor industrial reactors using electrical capacitance and impedance tomography – a hybrid approach

Indexed by: Web of Science Group

Grzegorz Kłosowski[a*], Tomasz Rymarczyk[b], Konrad Niderla[b], Monika Kulisz[a], Łukasz Skowron[a], Manuchehr Soleimani[c]

[a] Lublin University of Technology, Department of Organization of Enterprise, ul. Nadbystrzycka 38D, 20-618 Lublin, Poland
[b] WSEI University, ul. Projektowa 4, 20-209 Lublin, Poland, Research and Development Center, Netrix S.A.
[c] University of Bath, Department of Electronic & Electrical Engineering, Claverton Down, Bath, BA2 7AY, United Kingdom

Highlights

- Combination of two types of electrical tomography (capacitance and impedance).
- Verification of the advantage of hybrid tomography over homogeneous methods.
- Application of the LSTM network to solve the inverse problem in electrical tomography.
- The original approach to tomographic measurements as a data sequence for the LSTM network.

Abstract

The article presents a new concept for monitoring industrial tank reactors. The presented concept allows for faster and more reliable monitoring of industrial processes, which increases their reliability and reduces operating costs. The innovative method is based on electrical tomography. At the same time, it is non-invasive and enables the imaging of phase changes inside tanks filled with liquid. In particular, the hybrid tomograph can detect gas bubbles and crystals formed during industrial processes. The main novelty of the described solution is the simultaneous use of two types of electrical tomography: impedance and capacitance. Another novelty is the use of the LSTM network to solve the tomographic inverse problem. It was made possible by taking the measurement vector as a data sequence. Research has shown that the proposed hybrid solution and the LSTM algorithm work better than separate systems based on impedance or capacitance tomography.

Keywords
electrical tomography, industrial systems, process control, LSTM networks, machine learning

1. Introduction

Monitoring of industrial processes is an important condition for the effective operation of machines and devices and affects the reliability of both systems and processes [37]. Tank reactors are used in industrial processes based on chemical reactions. During the operation of a tank reactor, various physical and chemical reactions occur inside it, which may be accompanied by phase changes [14]. Considering that processes of this type are dynamic and may have an uneven distribution in relation to the volume of the tank, modelling the processes in question is difficult. Proper operation of tank reactors and entire industrial installations is a key factor in obtaining appropriate quality parameters for the processes. Therefore, industrial processes must be precisely monitored.

Industrial reactors are used in various branches of the economy. For example, in biogas plants, reactors are used to produce biogas from waste generated in wastewater treatment processes [1, 4, 9, 10]. Other areas of application of industrial reactors are: in the food industry for the production of yoghurt [2] or beer [39], in the paper industry [18], in the pharmaceutical industry [40], and in the chemical and petrochemical industry [16]. Tank reactors are vessels adapted to carry out controlled chemical reactions. Many such reactions take place inside industrial reactors. They can be controlled, for example, by changing the mixing frequency, changing the flow rate and speed, or controlling changes in pressure or temperature, as well as by selecting the appropriate substrate proportions. Process control is more difficult the more dynamic it is, which is why the response time of monitoring systems is of great importance. In addition to the parameters of the process, its course is also affected by the design of the industrial reactor: its diameter,

(*) Corresponding author.
E-mail addresses: G. Kłosowski (ORCID: 0000-0001-7927-3674) g.klosowski@pollub.pl, T. Rymarczyk (ORCID: 0000-0002-3524-9151) tomasz@rymarczyk.com, K. Niderla (ORCID: 0000-0003-1280-0622) konrad.niderla@netrix.com.pl, M. Kulisz (ORCID: 0000-0002-8111-2316) m.kulisz@pollub.pl, Ł. Skowron (ORCID: 0000-0002-9253-3474) l.skowron@pollub.pl, M. Soleimani (ORCID: 0000-0002-6341-9592) ms350@bath.ac.uk

shape, and capacity, as well as the material of the wall.

One of the groups of industrial reactors, taking into account the criterion of the aggregation state of the substrates, are heterogeneous reactors in which gas and liquid, gas and solid, and liquid and solid can coexist. We are dealing with the crystallisation process in the case of two-phase solid-liquid processes. Supervision—constant monitoring—is essential in industrial reactors where such processes occur. This type of monitoring aims to control the process of crystal precipitation. It is about obtaining answers to the questions of whether the process of phase transformations inside the reactor has been started, the places of crystal nucleation, and the current size of the crystals [43]. Thanks to this knowledge, actions can be taken to ensure the correct course of the process [26]. Therefore, the purpose of monitoring is to obtain precise information, in real-time, on the emerging crystals or gas bubbles and thus ensure the reliability of both the implemented processes as well as production systems or entire industrial installations [35, 36]. The registration of actual parameters carried out during process monitoring enables the calculation of deviations from optimal values. Maintenance services or automatic systems receive a signal to apply corrective actions if the limit deviations are exceeded. Thanks to early information from the monitoring system, it is possible to maintain the appropriate quality of processes and final products.

Monitoring industrial processes and systems using tank reactors is difficult. Due to the impossibility of non-invasive observation of the reactor interior, only basic physical parameters such as temperature, pressure, the angular velocity of the stirrer, or flow rate and velocity can be measured directly. However, these are point measurements. On their basis, it is possible to estimate, with some approximation, the condition of the reactor interior [12]. However, it is an indirect method with significant uncertainty in the inference, which is a disadvantage. A common drawback of monitoring methods based on traditional measurements is the need to use invasive sensors that can disturb process conditions. The general disadvantage of the classical methods is the point analysis, which concerns only selected fragments of the reactor interior. Tomography is the only known method that allows imaging entire sections of objects (2D) and spatial sections (3D). Based on the information provided by various sensors located throughout the analyzed industrial installation, SCADA systems are an example of a traditional approach to process monitoring [7, 23, 28].

Among the conventional measurement techniques of parameters describing the state of the process described in the literature, the following can be distinguished: visual observations, liquid crystal thermography, colourimetric methods, the conductivity probe method, and the planar laser-induced fluorescence method. The visual observation technique provides only a rough approximation of the measured parameters without quantification. Colourimetric methods rely on using two acid-base indicators and their color change properties due to chemical reactions, combined with colorimetric diagnostics of digital images extracted from video recorded during the process [6]. The method of liquid crystal thermography used, among others, by Lee and Vianneskis is based on the change of color of liquid crystals because of temperature change [20]. The disadvantages of both of these methods are that the monitored reactor must be transparent, which significantly hinders their use on an industrial scale. In the planar laser fluorescence technique, a fluorescent indicator is used as a tracer, and the change in the dependence of fluorescence intensity on temperature and dye concentration is used. In addition, this method requires a light source, i.e., a laser, which can illuminate the selected section. This method is non-invasive but limited only to small tanks due to the high laser power required for larger volumes [6]. The last of the techniques discussed are the conductivity probe method, which is based on the difference in electrical resistance between the vapour and liquid phases. The method uses a probe or single-point sensor. Unfortunately, the probe can only measure local conductivity, and the calculated process parameters depend on the probe's position. Therefore, this technique does not apply at higher temperatures or industrial reactors [25].

Due to the limitations of invasive methods of process monitoring, more and more attempts are being made to use non-invasive tomographic methods, i.e., electrical capacitance tomography (ECT) [24, 44, 45, 47], electrical impedance tomography (EIT) [10, 11, 22, 29, 41], magnetoacoustic tomography [48, 49], electrical resistance tomography [27, 38, 46], ultrasonic tomography [19, 21, 31], or computed tomography using radiation X [3, 30].

Monitoring processes using tomography, unlike point methods, allows one to visualize the inside of industrial tank reactors without disturbing the process because the sensors are placed outside the tank. Tomography allows imaging of the boundaries between the various components inside the reactor in real-time, allowing the observation of changes' dynamics. In addition, tomography is a relatively cheap solution, which fact supports the legitimacy of its use. The presented study aimed to verify the effectiveness of hybrid tomography based on simultaneous EIT+ECT measurements. Therefore, the heterogeneous (heterogeneous, hybrid) tomographic method (EIT+ECT) was compared with the homogeneous (homogenous) methods, EIT and ECT. The presented tomographic system uses a neural network with long-term memory (LSTM). This approach is a novelty in tomography, and in combination with the hybrid nature of the EIT+ECT tomograph, it brings a new quality to the current state of knowledge.

The structure of the work includes four chapters. The Materials and Methods chapter follows the introduction, which describes the test stand, consisting of a physical model of a tank reactor and a tomograph with electrodes. The algorithmic methods used are also discussed. The third part, entitled Results, presents various reconstruction images obtained based on simulation data and real measurements from the physical model of the reactor. Quantitative indicators assessing the quality of imaging are also presented. The last part, Discussion and Conclusions contains a short analysis and summary of the results obtained and assumptions from the research, as well as directions for future work.

2. Materials and Methods

This section contains a description of the models used in the research. The main object of the research was a physical model of a tank reactor to which EIT and ECT electrodes were

connected and a prototype of a hybrid tomograph enabling simultaneous EIT and ECT measurements. The digital model concerned an algorithm based on the LSTM network, which solved the inverse problem, and the spatial image of the tank, which was the distribution of the electrical conductivity of individual voxels that are components of the finite element mesh.

2.1 Hardware

The subject of the research was a physical model of a tank reactor. A hybrid tomograph prototype with electrodes was used for the research, adapted to process simultaneous or separate EIT and/or ECT measurements, which was entirely designed and manufactured in the Nertix SA laboratory. The hybrid tomograph combines two measurements: voltage measurement as part of EIT and capacitance measurement as part of ECT. The main limitation of the measurement speed was the period of the generated signal. Theoretically, a measurement time of 16 ms can be achieved. A 1 kHz signal is 1 ms per electrode multiplied by 16 electrodes. However, the measurement sampling period is longer and amounts to slightly less than 100 ms. This is because a dead period is used due to the need to stabilize the current after switching the excitation from one pair of electrodes to the other.

The tomograph in question was built based on a set of Intel Altera Cyclone IV and Cyclone V FPGA chips, which allowed the use of parallel function blocks independent of each channel. The tomograph consists of the main board with a power supply and an excitation current controller, measurement cards, and a data controller with an image reconstruction algorithm. The motherboard serves as a connection for data buses and addresses buses for individual blocks. A power supply unit on the motherboard converts the 12 V DC voltage (from the battery) into the voltage required to operate individual function cards properly. In addition, the battery control and charging system have been integrated into the power supply unit. The main board acts as a generator of the excitation current signal and contains a system for verifying the signal's correctness and the electrode connection's correctness. Another element of the tomograph is the measurement card, which consists of four active electrodes containing blocks for forming the measured signal along with the gain control and detection of the zero intersection point—the voltage measured with the x-axis, which is necessary, among others, to determine the length of the wavelength and phase shift. Together with the Cyclone IV FPGA system and the A/D converter, the ADS8588 system performs the measurement function, including the signal filtering process, calculating the RMS value, and measuring the signal phase. Then, the initial data prepared in this way is transferred to the control unit via buses. Eight Cyclone IV systems were used in the CT scanner. The last element of the hybrid tomograph is the data controller, which has a built-in dual-core ARM Cortex-A9 processor and collects data from individual measurement cards via FPGA blocks (Field Programmable Gate Array) on an Intel Altera Cyclone V. It transfers configuration data to individual measurement blocks and supervises the correctness of the measurements. The function of the user interface, together with the reconstruction mechanisms, is performed by a processor operating under Linux. Measurement data is sent via Ethernet to the control unit, which is stored in mass memory. Real-time image reconstruction is also possible.

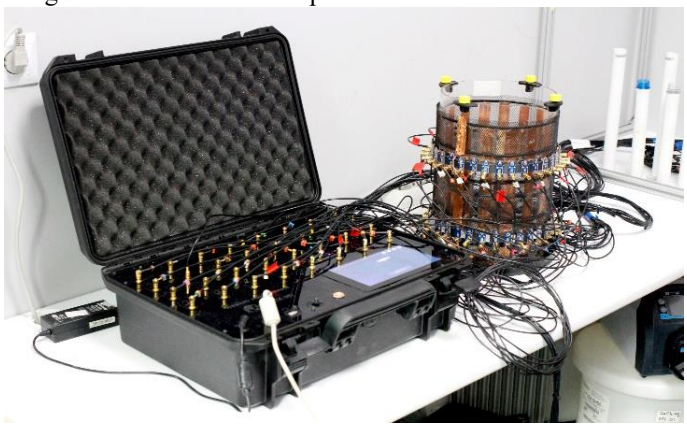

Figure 1. Hybrid tomograph connected to a tank surrounded by EIT and ECT electrodes.

The tank shown in Figure 1 has two rings of electrodes, upper and lower. Only the lower ring was used in the study, which consisted of 16 EIT electrodes and 16 ECT electrodes. Figure 2 shows a close-up of the EIT and ECT electrodes. ECT electrodes are hermetically sealed, i.e., isolated from the liquid filling the tank.

(a)

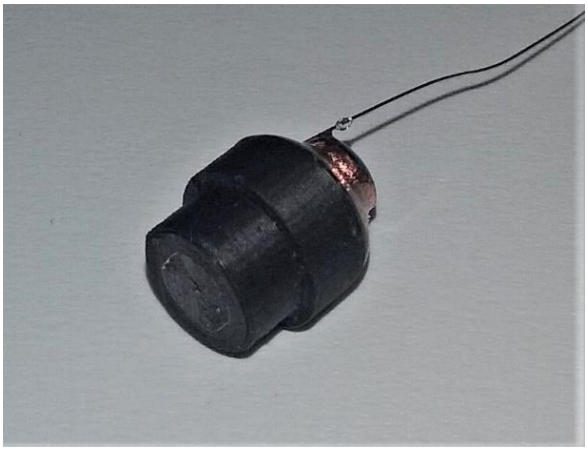

(b)

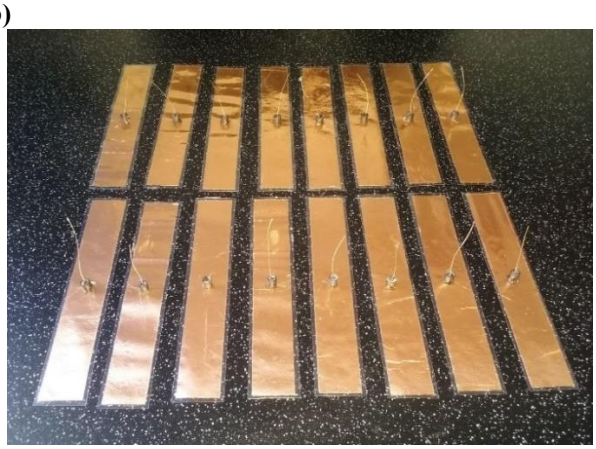

Figure 2. Tomographic electrodes: (a) - a single EIT electrode, (b) - a set of 16 ECT electrodes.

All elements of the prototype tomographic system, including the tomograph, electrodes, and tank, were designed and manufactured in the laboratories of Netrix SA.

2.2 Simulation Environment

Electrical tomography is inextricably linked with the need to solve the inverse problem. It is the basic difficulty and, at the same time, the challenge that accompanies this non-invasive, non-destructive technique of imaging the interiors of objects. The inverse problem is related to the deficit of input information (independent variables) compared to the output variables (observations), which results in the uncertainty of the obtained solution. Because we are attempting to deduce the cause from the effects, the inverse problem is synonymous with the ill-posed problem. The presented research is about identifying the internal structure of the tested object (a pipeline, tank, or reactor) based on voltage and/or capacitance measurements from electrodes placed outside and around its walls. An easier and unambiguously solved forward problem (the forward problem) consists in calculating the voltages on the electrodes applied to the surface of the tested object based on known mathematical models that take into account the geometry and structure of the object and material parameters. In the case of EIT, a forward problem can be represented as a potential distribution calculated by the Laplace partial differential equation using relation (1) [32]

$$\nabla \cdot (\sigma \nabla u) = 0 \tag{1}$$

where $\sigma = \sigma(S)$ is spatial conductivity, $S = (x_1, x_2, x_3)$ is a vector of spatial coordinates, and ∇u is a potential function. The forward problem is to solve the potential function ∇u using the known conductivity $\sigma(S)$ while accounting for boundary conditions in homogeneous environments where $\sigma = const$. In heterogeneous environments, the generalized Laplace equation (2) applies

$$\sum_{i=1}^{3} \frac{\partial}{\partial x_i}\left(\sigma \frac{\partial u}{\partial x_i}\right) = 0 \quad \text{for} \quad \frac{\omega \varepsilon}{\sigma} \ll 1 \tag{2}$$

where ω is the frequency of the current and ε is the permittivity. Using the EIT hardware system, when voltages are applied, and the associated currents are detected at the L electrodes, we apply Dirichlet to Neumann (DtN) mapping. DtN mapping is used to determine boundary conditions using the formula $u|_{\partial\Psi} \longrightarrow \left(\sigma \frac{\partial u}{\partial \boldsymbol{n}}\right)\Big|_{\partial\Psi}$, where $\boldsymbol{n}$ is the outer normal vector. If Λ_σ is the Dirichlet to Neumann transformation operator, then the EIT inverse problem is to find the parameter σ from Λ_σ. A forward problem in electrical capacitance tomography (ECT) is described by the Poisson equation (3)

$$\nabla.\left(\varepsilon(x_1, x_2, x_3)\nabla\varphi(x_1, x_2, x_3)\right) = -\rho(x_1, x_2, x_3) \tag{3}$$

where $\varepsilon(x_1, x_2, x_3)$ represents the permittivity distribution in the tested section, $\varphi(x_1, x_2, x_3)$ – the electric potential distribution, and $\rho(x_1, x_2, x_3)$ represents the electric charge distribution [8]. Formula (3) defines the relationship between the capacitance measurements and the permittivity distribution. The free charges of the reconstructed fragment are zero in ECT. When $\rho(x_1, x_2, x_3) = 0$, relation (3) is converted to the Laplace equation, which should be used in boundary conditions. A forward problem in ECT can be efficiently solved using the finite element method (FEM). FEM is a numerical method that calculates the values of basic functions for individual elements of the FEM mesh. After determining the charges on the receiving electrode, the capacitance can be determined from Gauss's law according to equation (4)

$$C_{i,j} = \frac{Q}{V} = \frac{1}{\Delta V_{i,j}} \oint_{\Gamma_j} \varepsilon(x_1, x_2, x_3)\nabla\varphi(x_1, x_2, x_3) d\Gamma_j \tag{4}$$

where Q denotes the electric charges on the electrodes, $\Delta V_{i,j}$ denotes the difference in electric potential between the tested object's surface and the measuring electrodes, and Γ_j is the surface of the j-th electrode. The task of the simulation environment is correctly mapping real conditions based on algorithmic models. It is particularly important when generating the simulation data necessary to train machine learning models. The Eidors toolbox, cooperating with the Matlab software [34], was used to develop the simulation environment. With its help, the FEM method was implemented, thanks to which meshes of tetrahedral finite elements (voxels) were made. Figure 3 shows how to generate the EIT measurements and observations to train the neural network. For this purpose, a forward problem was solved by transforming the conductivity distribution (Figure 3b) into a vector of 96 voltage measurements (Figure 3c) measured between individual pairs of electrodes. A digital, virtual model of the tank was developed, describing the geometry and material characteristics of the tested object together with the electrodes surrounding it. The key element of the model is the spatial mesh of finite elements on which the tomographic image is created. The FEM model (Figure 3b) has a lower height than the tank shown in Figure 3a because only the lower electrode ring of the tank was used in the tests.

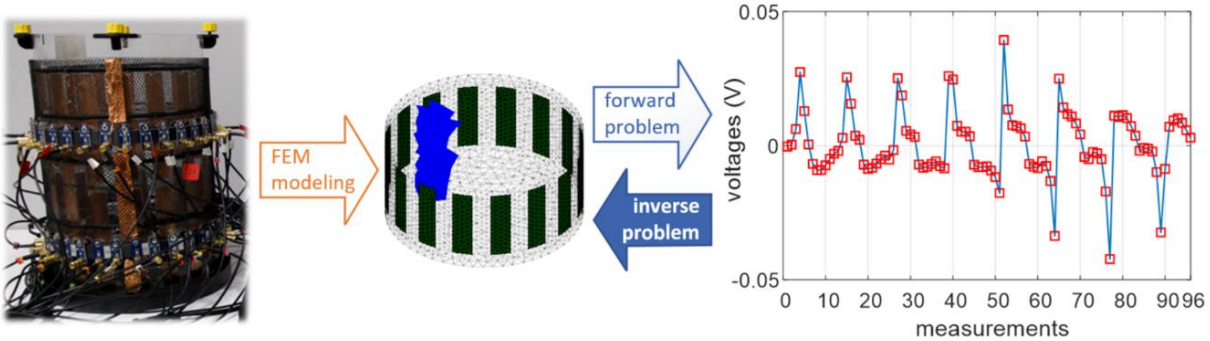

Figure 3. The essence of the forward and inverse problem in the EIT: (a) - a physical model of the tank, (b) - a FEM model, (c) - measurement values.

Based on the FEM model, pattern images were generated by assigning appropriate conductivity or electric capacitance values to individual finite elements (voxels). In the tested case, a tank with an outer diameter of ø200 mm (Figure 3a) contains tap water, the conductivity of which oscillates around 500 µS/cm. Plastic tubes with a diameter of ø20 mm, filled with air, were immersed in the water. ECT measurements were generated similarly, while EIT+ECT measurements were obtained by combining two measurement vectors for the EIT and ECT methods. The method of combining EIT and ECT measurements in the algorithmic scheme of the tomographic system is shown in Figure 4. From left to right, the ECT and EIT measurement vectors, with 120 and 96 measurements, are combined into one vector with 216 measurements. These measurements are the inputs of the LSTM neural network, which outputs a vector of 20,445 individual FEM voxel values. The last stage is transforming the output vector into a tomographic image. Figure 4 shows how to solve the inverse tomography problem using hybrid measurements and the LSTM network.

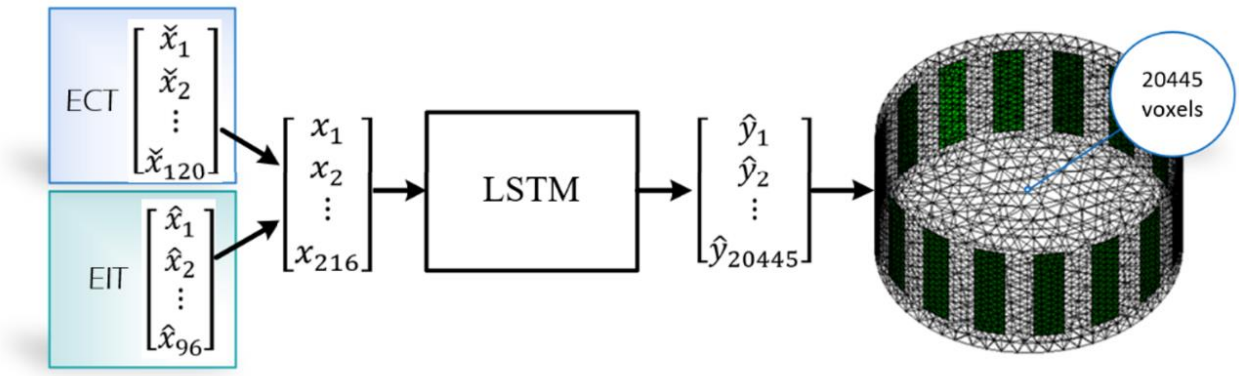

Figure 4. Diagram of a hybrid tomographic system for 3D spatial imaging.

2.3 LSTM Network Architecture

Based on simulation data, three independent LSTM systems were trained for three types of tomographs: homogeneous EIT and ECT and hybrid EIT+ECT. For the three types of input data (measurements), EIT, ECT, and EIT+ECT, identical reconstructions (master images) were assigned. Scripts for generating simulation cases have been validated based on real measurements. Thirty thousand cases were used to train the LSTM network, from which 1,000 were extracted as a validation set. The network was trained using a popular optimization algorithm called ADAM (Adaptive Moment Estimation). ADAM performs well in tasks with a large training set and models with many parameters. By design, ADAM is an algorithm designed to train and optimize deep neural networks. Based on the mean and variance of the gradient, the algorithm calculates the learning rate values. These coefficients are then used to update the hyperparameters of the LSTM network. The validation set was used to stop the neural network's learning. A stop occurred when the RMSE error for the validation set did not decrease for 6 consecutive iterations. The entire training set was divided into mini-batches with a size of 500 observations. Thus, a single epoch consisted of 58 iterations (29000/500). The validation error was calculated after every 30 iterations performed on the training set. The learning rate was constant and equaled $\alpha = 10^{-3}$. There are no strict recommendations regarding the design of neural network architecture, meaning it must be selected manually. The network's hyperparameters include, among others, the number and type of layers, the number of units hidden in the layers, transfer functions, learning rate, size of mini-batches of data, type of learning algorithm, and other parameters, which were selected empirically. The network structure for EIT+ECT hybrid inputs is shown in Table 1.

Table 1. LSTM network architecture - heterogeneous case (EIT+ECT).

Layer No.	Layer description	Number of activations	Learnable – variable parameters	Total number of learnable
1	Sequence layer with 216 inputs	216	-	0
2	LSTM layer with 5000 hidden units	5000	Input weights: 20000×216 Recurrent Weights: 20000×5000 Bias: 20000×1	104340000
3	Normalization of mini-batches	5000	Offset: 5000×1 Scale factor: 5000×1	10000
4	1-D global max pooling layer	5000	-	0
5	Fully connected layer with 20445 outputs	20445	Weights: 20445×5000 Bias: 20445×1	102245445
6	Regression layer with mean squared error as a quality criterion	20445	-	0

The first layer on all models is the sequential input layer. For EIT, the input layer is a vector with 96 values. For ECT, there

are 120 inputs, and for hybrid EIT+ECT, it is a vector of 216 mixed measurements. Next is the bi-directional LSTM layer, which learns long-term correlations between signal time steps or sequence data. The state of the LSTM layer consists of a cell state and a hidden state. The first one contains information obtained from previous time intervals, so each step adds or removes information about the cell's state. The hidden state contains the layer's output in a given time step t; therefore, this state is also called the output state. Gates controls changes in these states. The gate that controls the cell state update level is the entry gate (i), the gate that controls the cell state reset level is the forget gate (f), the gate that adds information to the cell state is the cell candidate (g), and the gate that controls the cell state level added to the hidden state is the output gate (o). Figure 5 illustrates how the gates control LSTM layer state changes, interact with each other, update layer states, and provide additional cell state information.

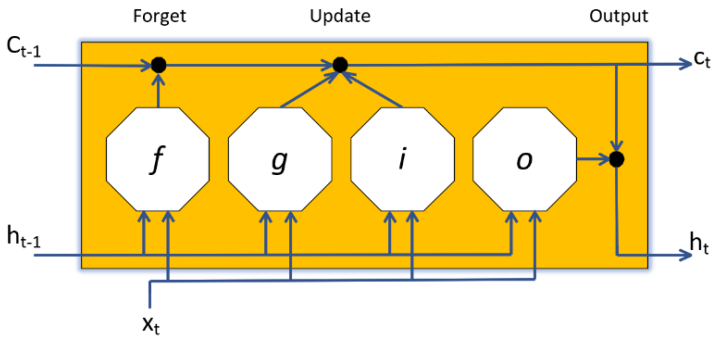

Figure 5. Data flow in a single LSTM sequential step [5].

Each gate can be characterized by input weights (W), recursive weights (R), and biases (b), as shown in the matrix below:

$$W = \begin{bmatrix} W_i \\ W_f \\ W_g \\ W_o \end{bmatrix}, R = \begin{bmatrix} R_i \\ R_f \\ R_g \\ R_o \end{bmatrix}, b = \begin{bmatrix} b_i \\ b_f \\ b_g \\ b_o \end{bmatrix},$$

The state of the cell at a given time step t is denoted by $c_t = f_t \odot c_{t-1} + i_t \odot g_t$, where $\odot$ is the Hadamard product representing vector multiplication. The hidden state is defined as $h_t = o_t \odot \sigma_c(c_t)$, where the activation function of the state is σ_c. Therefore, each of the gates can be defined in a given time step t as follows: input gate $i_t = \sigma_g(W_i x_t + R_i h_{t-1} + b_i)$, forgetting gate $f_t = \sigma_g(W_f x_t + R_f h_{t-1} + b_f)$, candidate gate $g_t = \sigma_c(W_g x_t + R_g h_{t-1} + b_g)$ and exit gate $o_t = \sigma_g(W_o x_t + R_o h_{t-1} + b_o)$. For each of the three networks (EIT, ECT, EIT+ECT), the LSTM layer contained 5,000 hidden units. The activation function to update the cell and the hidden state is the hyperbolic tangent (tanh) function, and the activation function to apply to gates is the sigmoid function $\sigma(x) = (1 + e^{-x})^{-1}$The function to initialize the weights is an orthogonal matrix defined by the QR decomposition with Z = QR for a random matrix Z coming from the unit normal distribution. The function for initializing input weights for all models is a Glorot-type initializer, enabling effective weight value assignment. The problem of appropriate, random initialization of weights is important because, when training deep neural networks, a fading or rapidly increasing gradient is a big problem. In order to avoid this, the algorithm should choose the weights so that the variance of the outputs and inputs of a given layer is the same. In addition, the gradients before passing through a given layer and after the backpropagation procedure of gradients should have equal variance. In the described studies, the Glorot initialization algorithm initializes the weights by drawing them independently from a homogeneous distribution with a mean of zero [17]. The next layer is the mini-batch normalization layer, which normalizes the input data across all processed cases. The normalization layer transforms the xi elements of the input signal in such a way that it first calculates the mean μ_B and the variance σ_B^2. Then, normalized activations $\hat{x}_i$ are calculated as (5)

$$\hat{x}_i = \frac{x_i - \mu_B}{\sqrt{\sigma_B{}^2 + \varepsilon}} \tag{5}$$

where ε is a constant intended to improve numerical stability if the variance is very small. The mini-batch normalization algorithm takes into account the eventuality that the mean is zero and/or the variance is unitary. These kinds of cases are not optimal for operations that follow mini-batch normalization. In the next step, activations are scaled using transformations (6)

$$y_i = \gamma \hat{x}_i + \beta \tag{6}$$

where β – offset and γ – scaling factor are learnable and updated during the training of the neural network. The next layer is a 1-D global maximization pooling layer that downsizes the inputs, returning only the maximum values extracted from specific groups of voxels. The penultimate layer is the fully connected layer with 20,445 outputs, which multiplies the input data by the weight matrix and then adds the bias vector. The Glorot function was used to initialize the weights in this layer in all trained LSTM network models. The last one is the regression layer, whose main task is calculating the mean squared error value. For a single observation, the root mean square error (RMSE) is given by (7).

$$RMSE = \sqrt{\sum_{i=1}^{R} \frac{(\hat{y}_i - y_i)^2}{R}} \tag{7}$$

where R is the number of responses, $\hat{y}_i$ is the target score, andy_i is the network prediction for the i-th response [42].

Figure 6 shows the course of the LSTM network learning process. The quality assessment criterion is RMSE. The shape of the graph, the lack of clear fluctuations, and the consistency of the RMSE errors for the validation and training sets indicate a lack of overfitting and give grounds to expect that the neural network has gained the ability to generalize.

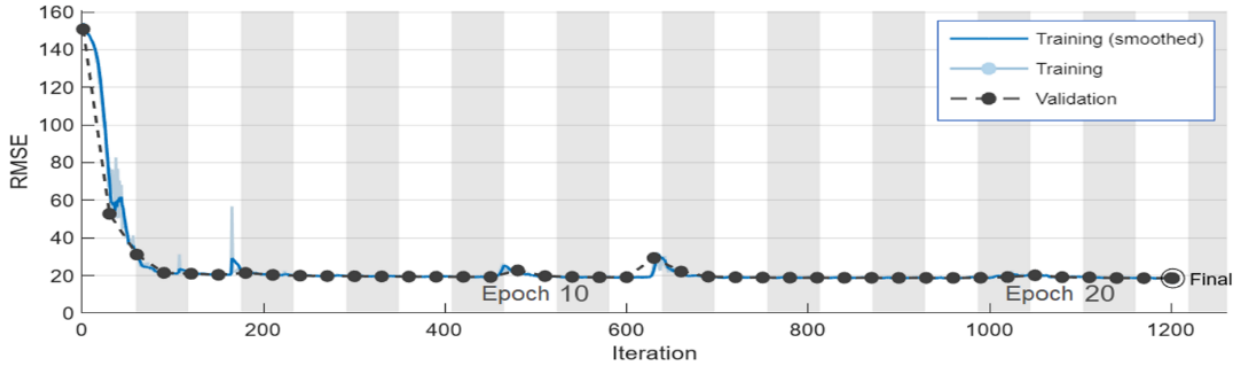

Figure 6. The performance of the LSTM network learning process in relation to the RMSE.

3. Experimental Results

Figure 7 compares reconstructions obtained using the hybrid EIT+ECT method with tomograms obtained using homogeneous EIT and ECT methods. It is a comparison based on synthetically generated cases because only such cases have reference images that can be used to train neural networks and quantitatively verify the reconstructed images' quality.

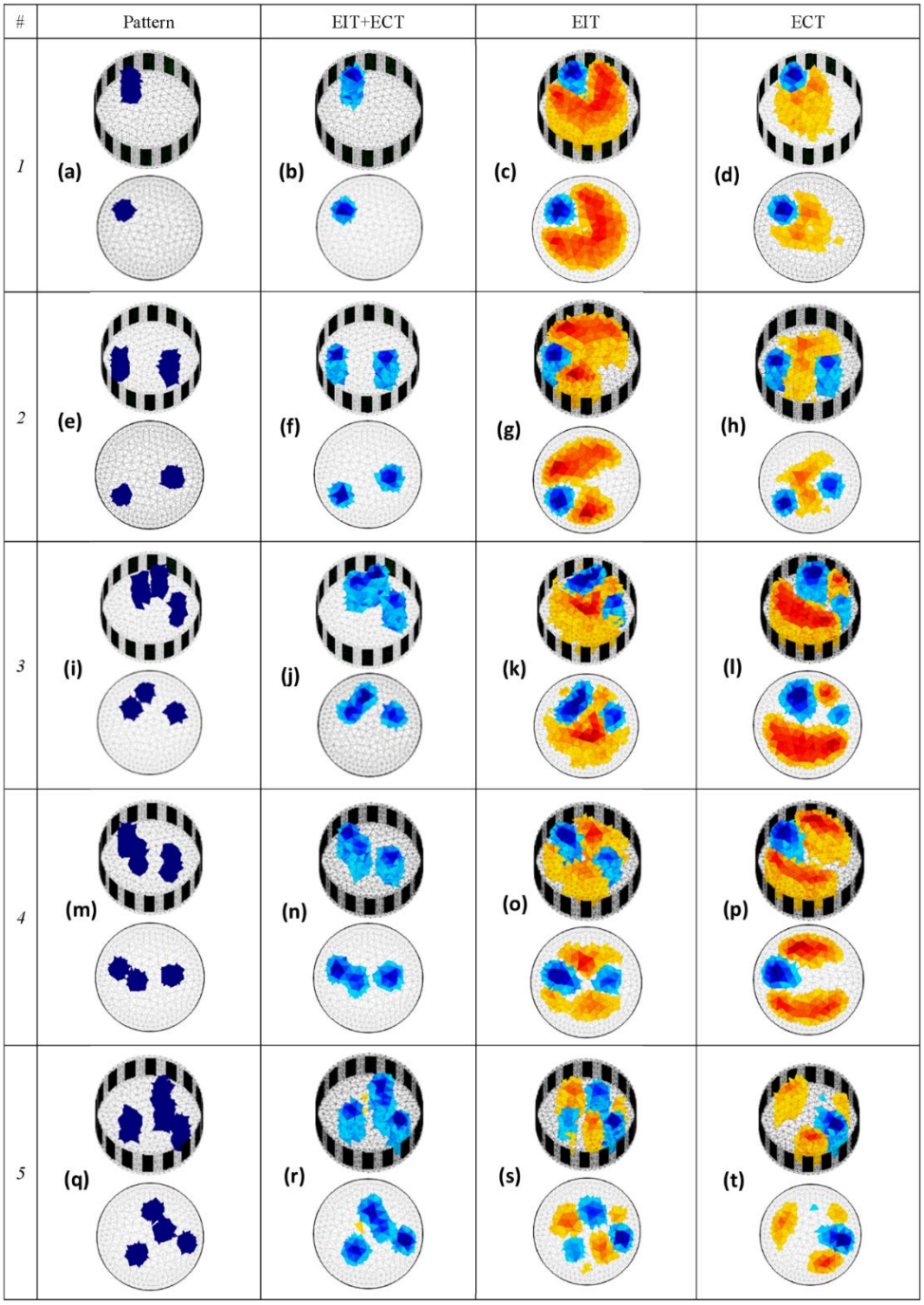

Figure 7. Comparison of the results obtained with the EIT and ECT homogeneous methods with the EIT+ECT heterogeneous method.

Five representative cases were selected for comparison. Each reconstruction is presented in two views - axonometric and upper. The first column contains reference images. In the following columns are reconstructions made with the EIT+ECT (hybrid) and homogeneous EIT and ECT methods. In this way, the effectiveness of the hybrid method can be assessed. It can be noted that cases with a small number of inclusions are reconstructed better than those with a larger number of inclusions. Analyzing cases #1(a-d), a single inclusion is well reconstructed even by homogeneous methods, and the differences concern only the background color. However, in the case of #2(g), the EIT method fails because the reconstruction does not show one of the tubes. Case #3(l) is worse than the others because it cannot distinguish inclusions that are close to each other. Case #4(p) omits the right inclusion, and #4(o) poorly demarcates adjacent inclusions. Similar problems occur on reconstructions #5(s-t). It is visible that the reconstructions obtained with the hybrid method (EIT+ECT) #1(b), #2(f), #3(j), #4(n), #5(r) are of better quality than the reconstructions obtained with homogeneous methods.

Quantification was based on three popular quality metrics used to estimate image quality, requiring reference images. The first indicator is the mean square error (MSE), defined as (8)

$$MSE = \sum_{i=1}^{R} \frac{(t_i - y_i)^2}{R}, \tag{8}$$

which is very similar to the RMSE described earlier in formula (7). The peak signal-to-noise ratio (PSNR) is determined by the formula (9) [13]

$$PSNR = 10 \cdot \log_{10}(R^2/MSE) \tag{9}$$

where R is the maximum fluctuation of the voxel value of the input image, which in this case is R = 1. The PSNR calculates the peak signal-to-noise ratio of the reconstruction image. The higher the PSNR value, the better the image quality. Another indicator used for the assessment is the structural similarity index (SSIM) [15]. A characteristic feature of SSIM is the combination of three features in one indicator: contrast, local image structure, and luminance. The term "structures" herein means patterns of voxel intensity that include immediately adjacent voxels. Structures are normalized for luminance and contrast. Since the human visual system is adapted to observe structural differences, the SSIM quality index is consistent with the subjective assessment of a human being, which is particularly desirable in the case of tomography. The $SSIM(\hat{y}, y)$ indicator is defined by the formula (10)

$$SSIM = \frac{(2\mu_{\hat{y}}\mu_{\mathrm{y}} + \mathrm{C}_1)(2\sigma_{\hat{y}y} + \mathrm{C}_2)}{(\mu_{\hat{y}}^2 + \mu_{\mathrm{y}}^2 + \mathrm{C}_1)(\sigma_{\hat{y}}^2 + \sigma_{\mathrm{y}}^2 + \mathrm{C}_2)} \tag{10}$$

where $\mu_{\hat{y}}, \mu_y, \sigma_{\hat{y}}, \sigma_y \; i \; \sigma_{\hat{y}y}$ are the local means, standard deviations, and cross-covariances for images $\hat{y}$, y; $C_1 = (0.01 \cdot L)^2$ and $C_2 = (0.03 \cdot L)^2$; if the voxel values are in the range (0,1), then L=1 in this case. The last measure used in these studies is the image correlation coefficient (ICC), which is calculated according to the formula (11) [33]

$$\mathrm{ICC} = \frac{\sum_{i=1}^{n}(y_i - \bar{y})(\hat{y}_i - \bar{\hat{y}})}{\sqrt{\sum_{i=1}^{n}(y_i - \bar{y})^2 \sum_{i=1}^{n}(\hat{y}_i - \bar{\hat{y}})^2}} \tag{11}$$

where $\bar{y}$ is the distribution of average voxel values of the reference image, $\bar{\hat{y}}$ is the distribution of average voxel values of the reconstructed voxels.

Table 2 presents the values of four indicators related to the three methods tested and five reconstructive cases. The quantitative results generated by the metrics are consistent with the subjective and qualitative assessments resulting from the image analysis in Figure 7. In all tested configurations of four indices, three tomographic methods and five reconstruction cases, the EIT+ECT hybrid method always performs better than the other two homogeneous methods. In order to finally validate the usefulness of the EIT+ECT hybrid tomographic system, equipped with an algorithm based on the LSTM network, whose task is to transform measurements into spatial (3D) images, a number of reconstructions were carried out using a real (physical) model.

Table 2. Comparison of reconstruction quality indices.

Indicator of reconstruction quality		Reconstruction cases					Average
		#1	*#2*	*#3*	*#4*	*#5*	
EIT	MSE	0.1666	0.1355	0.1220	0.0944	0.1080	0.1253
	PSNR	7.7821	8.6781	9.1360	10.248	9.6655	9.1020
	SSIM	0.2744	0.2893	0.3042	0.3122	0.3016	0.2963
	ICC	0.3632	0.3438	0.3375	0.3553	0.4318	0.3663
ECT	MSE	0.4374	0.4030	0.1084	0.1324	0.0981	0.2359
	PSNR	3.5905	3.9468	9.6466	8.7787	10.082	7.2090
	SSIM	0.2157	0.2227	0.2110	0.2217	0.2282	0.2198
	ICC	0.5661	0.6178	0.5410	0.5036	0.5746	0.5606
EIT + ECT	MSE	0.0065	0.0181	0.0293	0.0239	0.0358	0.0227
	PSNR	21.828	17.422	15.317	16.213	14.461	17.048
	SSIM	0.7151	0.6213	0.6233	0.6222	0.5843	0.6332
	ICC	0.8624	0.8565	0.8121	0.8051	0.8050	0.8282
Is the MSE of the hybrid EIT+ECT algorithm the smallest?		Yes	Yes	Yes	Yes	Yes	Yes
Is the PSNR of the hybrid EIT+ECT algorithm the largest?		Yes	Yes	Yes	Yes	Yes	Yes
Is the SSIM of the EIT+ECT hybrid algorithm the largest?		Yes	Yes	Yes	Yes	Yes	Yes
Is the ICC of the hybrid EIT+ECT algorithm the largest?		Yes	Yes	Yes	Yes	Yes	Yes

Figure 8 visualizes the averaged values of the indicators for easier comparison. In this context, Figure 8 corresponds to the last column of Table 2, entitled "Average." In the case of MSE, the area assigned to the EIT+ECT method is smaller than that of EIT and ECT. The areas of the remaining three indicators evaluating the hybrid method are, in turn, clearly larger than the analogous measures of homogeneous methods. The percentage proportions visible on the chart make it easier to see the size of these advantages.

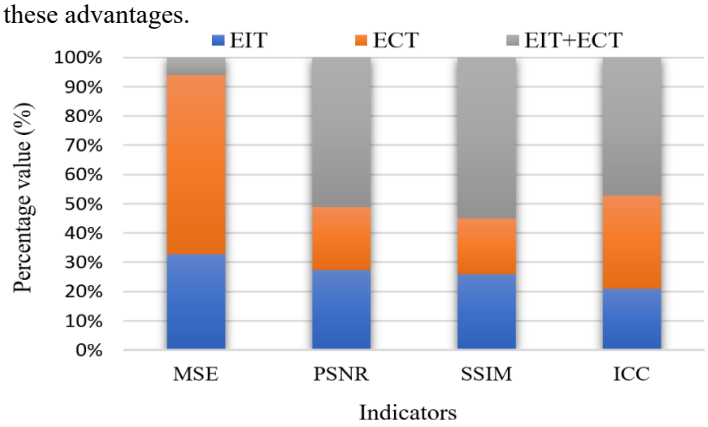

Figure 8. Average indicators of reconstruction quality.

Figure 9 shows five cases of different geometric configurations of immersion of the tubes in the water inside the tank. The first column in Figure 8 contains five photos of the test object taken from above. They show the location of the plastic pipes relative to the bottom. In the next two columns, there are reconstructions corresponding to real cases in the top and axonometric views. Comparing Figures 7 and 8, one can see a decrease in the quality of reconstructions obtained from real measurements compared to reconstructions made based on simulation measurements. The lower quality of the real reconstructions is caused by the noise in the measurement data and slightly different input data characteristics than the data used in the LSTM network learning process. There is always some level of noise during measurements. For example, the data used to train the network had 2% Gaussian noise, but the noise of this kind in real conditions may have slightly different parameters, resulting in worse reconstructions.

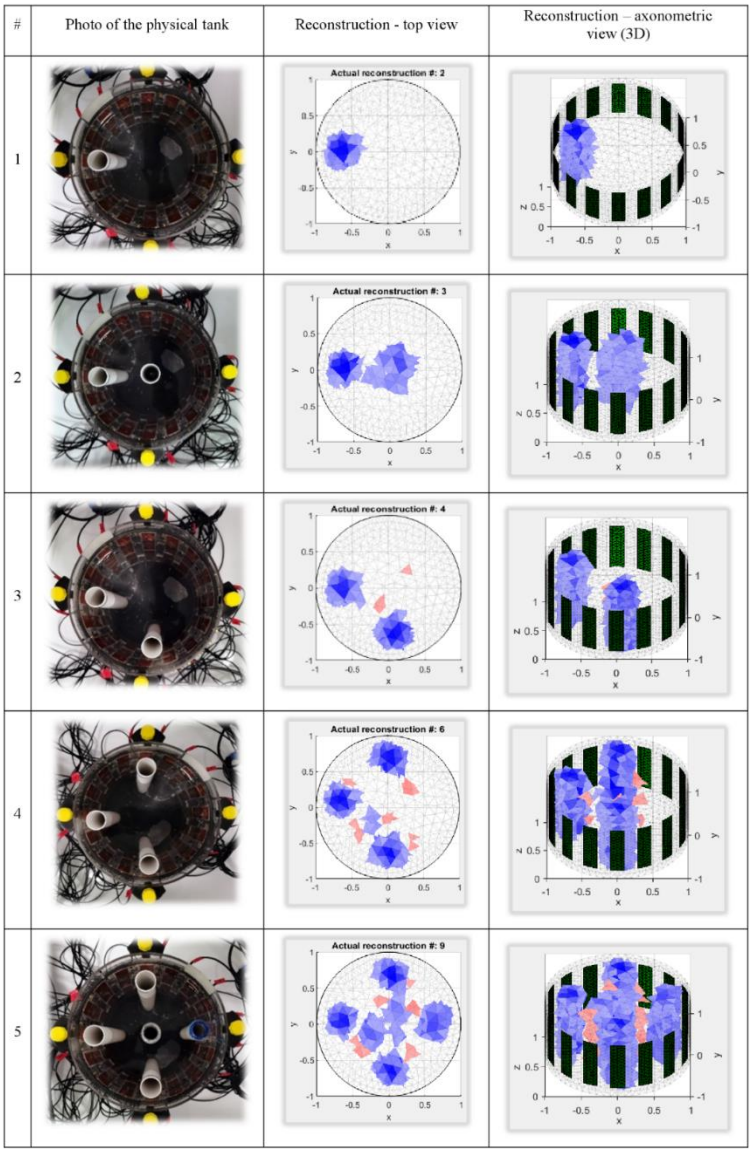

Figure 9. EIT+ECT imaging results in real conditions.

4. Discussion and Conclusions

The research described in this study aimed to verify the effectiveness and legitimacy of using EIT+ECT hybrid tomography. Innovation also used an algorithmic method of transforming measurements into images based on LSTM networks. To achieve the aim of the research, three independent predictive models were trained, including two homogeneous (EIT and ECT) and one hybrid (EIT+ECT), whose heterogeneous nature results from the combination of both methods mentioned above into one measurement vector. Combining EIT and ECT measurements into one vector increases the number of LSTM network inputs. When treated separately, the EIT and ECT methods functioned based on the number of measurements, respectively, of 96 and 120, while the input vector for the hybrid method was 216 measurements. This fact alone demonstrated the potential advantage of heterogeneous methods over homogeneous ones. The advantage of the hybrid method was confirmed by reconstructions based on simulation test cases and images based on measurements collected from electrodes applied to the surface of the physical reactor model. In addition, the effectiveness of the EIT+ECT method was verified based on the analysis of four image quality indices: MSE, PSNR, SSIM, and ICC. All indicators confirmed the superiority of the heterogeneous method over the homogeneous method. In addition to the appropriate algorithm tailored to the characteristics of the measurement data and the training set, the high quality of reconstruction depends on the use of appropriate equipment, from the tomograph to the electrodes. A prototype EIT/ECT hybrid tomograph was used in the study. The ECT electrodes were isolated from the liquid filling the tank reactor. The entire tomographic system with electronics was designed and manufactured in the Netrix SA laboratory. Future research will be conducted in adding ultrasonic tomography to the electrical tomography measurements. Enriching the measurement vector with non-electrical measurements should significantly expand the possibilities of using the new method in industrial tomography, as it will make the test object (e.g., an industrial reactor) independent of the current-voltage properties.

References

1. Admasu A, Bogale W, Mekonnen Y S. Experimental and simulation analysis of biogas production from beverage wastewater sludge for electricity generation. Scientific Reports 2022 12:1 2022; 12(1): 1–15, https://doi.org/10.1038/s41598-022-12811-3.
2. Aguirre-Ezkauriatza E J, Galarza-González M G, Uribe-Bujanda A I et al. Effect of Mixing During Fermentation in Yogurt Manufacturing. Journal of Dairy Science 2008; 91(12): 4454–4465, https://doi.org/10.3168/JDS.2008-1140.
3. Babout L, Grudzień K, Wiącek J et al. Selection of material for X-ray tomography analysis and DEM simulations: comparison between granular materials of biological and non-biological origins. Granular Matter 2018. doi:10.1007/s10035-018-0809-y, https://doi.org/10.1007/s10035-018-0809-y.
4. Banerjee S, Prasad N, Selvaraju S. Reactor Design for Biogas Production-A Short Review. Journal of Energy and Power Technology 2022, Vol. 4, 004 2022; 4(1): 1–22, https://doi.org/10.21926/JEPT.2201004.
5. Beale M H, Hagan M T, Demuth H B. Deep Learning Toolbox User's Guide. Herborn, The Mathworks Inc.: 2018.
6. Cabaret F, Bonnot S, Fradette L, Tanguy P A. Mixing Time Analysis Using Colorimetric Methods and Image Processing. Industrial and Engineering Chemistry Research 2007; 46(14): 5032–5042, https://doi.org/10.1021/IE0613265.
7. Chakraborty K, Choudhury M G, Das S, Paul S. Development of PLC-SCADA based control strategy for water storage in a tank for a semi-automated plant. Journal of Instrumentation 2020; 15(04): T04007, https://doi.org/10.1088/1748-0221/15/04/T04007.
8. Deabes W A, Abdelrahman M A. Solution of the forward problem of Electric Capacitance Tomography of conductive materials. WMSCI 2009 - The 13th World Multi-Conference on Systemics, Cybernetics and Informatics, Jointly with the 15th International Conference on Information Systems Analysis and Synthesis, ISAS 2009 - Proc., 2009.
9. Dębowski M, Zieliński M. Wastewater Treatment and Biogas Production: Innovative Technologies, Research and Development Directions. Energies 2022, Vol. 15, Page 2122 2022; 15(6): 2122, https://doi.org/10.3390/EN15062122.
10. Duraj A, Korzeniewska E, Krawczyk A. Classification algorithms to identify changes in resistance. Przeglad Elektrotechniczny 2015. doi:10.15199/48.2015.12.19, https://doi.org/10.15199/48.2015.12.19.
11. Dusek J, Mikulka J. Measurement-based domain parameter optimization in electrical impedance tomography imaging. Sensors 2021. doi:10.3390/s21072507, https://doi.org/10.3390/s21072507.
12. Dutz F J, Heinrich A, Bank R et al. Fiber-Optic Multipoint Sensor System with Low Drift for the Long-Term Monitoring of High-Temperature Distributions in Chemical Reactors. Sensors 2019, Vol. 19, Page 5476 2019; 19(24): 5476, https://doi.org/10.3390/S19245476.
13. Faragallah O S, El-Hoseny H, El-Shafai W et al. A comprehensive survey analysis for present solutions of medical image fusion and future directions. IEEE Access 2021; 9: 11358–11371, https://doi.org/10.1109/ACCESS.2020.3048315.
14. Fiderek P, Kucharski J, Wajman R. Fuzzy Regulator for Two-Phase Gas–Liquid Pipe Flows Control. Applied Sciences (Switzerland) 2022. doi:10.3390/APP12010399, https://doi.org/10.3390/APP12010399.
15. Fu W, Sheng Y, Xiong D. Optimal reconstruction design for JPEG-coded image using structural similarity index. Proceedings of the 2017 12th IEEE Conference on Industrial Electronics and Applications, ICIEA 2017 2018; 2018-February: 180–184, https://doi.org/10.1109/ICIEA.2017.8282837.
16. Gholami Z, Gholami F, Tišler Z, Vakili M. A Review on the Production of Light Olefins Using Steam Cracking of Hydrocarbons. Energies 2021, Vol. 14, Page 8190 2021; 14(23): 8190, https://doi.org/10.3390/EN14238190.
17. Glorot X, Yoshua B. Understanding the difficulty of training deep feedfor-ward neural networks. Proceedings of the thirteenth international confer-ence on artificial intelligence and statistics, 2010: 249–256.
18. Habets L H A, PAQUESWATERSYSTEMSB. V, Boerstraat T D. INTRODUCTION OF THE IC REACTOR IN THE PAPER INDUSTRY. 2001.
19. Koulountzios P, Rymarczyk T, Soleimani M. A quantitative ultrasonic travel-time tomography to investigate liquid elaborations in industrial processes. Sensors (Switzerland) 2019. doi:10.3390/s19235117, https://doi.org/10.3390/s19235117.
20. Lee K C, Yianneskis M. A Liquid Crystal Thermographic Technique for the Measurement of Mixing Characteristics in Stirred Vessels. Chemical Engineering Research and Design 1997; 75(8): 746–754, https://doi.org/10.1205/026387697524416.
21. Liang G, Dong F, Kolehmainen V et al. Nonstationary Image Reconstruction in Ultrasonic Transmission Tomography Using Kalman Filter and Dimension Reduction. IEEE Transactions on Instrumentation and Measurement 2021. doi:10.1109/TIM.2020.3031172,

https://doi.org/10.1109/TIM.2020.3031172.
22. Liu S, Huang Y, Wu H et al. Efficient Multitask Structure-Aware Sparse Bayesian Learning for Frequency-Difference Electrical Impedance Tomography. IEEE Transactions on Industrial Informatics 2021; 17(1): 463–472, https://doi.org/10.1109/TII.2020.2965202.
23. Moleda M, Momot A, Mrozek D. Regression methods for detecting anomalies in flue gas desulphurization installations in coal-fired power plants based on sensor data. Lecture Notes in Computer Science (including subseries Lecture Notes in Artificial Intelligence and Lecture Notes in Bioinformatics) 2020; 12141 LNCS: 316–329, https://doi.org/10.1007/978-3-030-50426-7_24/TABLES/3.
24. Mosorov V, Rybak G, Sankowski D. Plug Regime Flow Velocity Measurement Problem Based on Correlability Notion and Twin Plane Electrical Capacitance Tomography: Use Case. Sensors 2021, Vol. 21, Page 2189 2021; 21(6): 2189, https://doi.org/10.3390/S21062189.
25. Nguyen V T, Bui H. Development of Conductivity Probe and Signal Processing Algorithm for Measuring of Local Two-Phase Flow Parameters. VINANST-13: 13. Vietnam Conference on Nuclear Science and Technology; Hoi nghi Khoa hoc va Cong nghe Hat nhan Toan quoc lan thu 13 (1) 2019: 51079304.
26. Öner M, Bach C, Tajsoleiman T et al. Scale-up Modeling of a Pharmaceutical Crystallization Process via Compartmentalization Approach. Computer Aided Chemical Engineering 2018; 44: 181–186, https://doi.org/10.1016/B978-0-444-64241-7.50025-2.
27. Rao G, Aghajanian S, Koiranen T et al. Process monitoring of antisolvent based crystallization in low conductivity solutions using electrical impedance spectroscopy and 2-D electrical resistance tomography. Applied Sciences (Switzerland) 2020. doi:10.3390/app10113903, https://doi.org/10.3390/app10113903.
28. Rashad O, Attallah O, Morsi I. A smart PLC-SCADA framework for monitoring petroleum products terminals in industry 4.0 via machine learning. Measurement and Control (United Kingdom) 2022; 55(8): 830–848, https://doi.org/10.1177/00202940221103305/ASSET/IMAGES/LARGE/10.1177_00202940221103305-FIG2.JPEG.
29. Ricard F, Brechtelsbauer C, Xu X Y, Lawrence C J. Monitoring of multiphase pharmaceutical processes using electrical resistance tomography. Chemical Engineering Research and Design 2005. doi:10.1205/cherd.04324, https://doi.org/10.1205/cherd.04324.
30. Romanowski A, Łuczak P, Grudzień K. X-ray imaging analysis of silo flow parameters based on trace particles using targeted crowdsourcing. Sensors (Switzerland) 2019. doi:10.3390/s19153317, https://doi.org/10.3390/s19153317.
31. Rybak G, Strzecha K, Krakós M. A New Digital Platform for Collecting Measurement Data from the Novel Imaging Sensors in Urology. Sensors 2022. doi:10.3390/S22041539, https://doi.org/10.3390/S22041539.
32. Rymarczyk T, Kłosowski G, Hoła A et al. Comparison of Machine Learning Methods in Electrical Tomography for Detecting Moisture in Building Walls. Energies 2021; 14(10): 2777, https://doi.org/10.3390/en14102777.
33. Rymarczyk T, Kłosowski G, Hoła A et al. Optimising the use of Machine learning algorithms in electrical tomography of building Walls: Pixel oriented ensemble approach. Measurement 2022; 188: 110581, https://doi.org/10.1016/J.MEASUREMENT.2021.110581.
34. Rymarczyk T, Kozłowski E, Kłosowski G. Electrical impedance tomography in 3D flood embankments testing – elastic net approach. Transactions of the Institute of Measurement and Control 2019; 42(4): 680–690, https://doi.org/10.1177/0142331219857374.
35. Rząsa M R. Measurement of parameters of the moving gas bubbles with the image tomograph. 11th IMEKO TC14 Symposium on Laser Metrology for Precision Measurement and Inspection in Industry, LMPMI 2014 2014: 247–252.
36. Rząsa M R. Selection of optical tomography parameters for gas bubble shape analysis. Chemical and Process Engineering - Inzynieria Chemiczna i Procesowa 2014; 35(1): 19–33, https://doi.org/10.2478/CPE-2014-0002.
37. Sankowski D, Plaskowski A, Mosorov V et al. Image segmentation algorithms for industrial process tomography. 2nd World Congress on Industrial Process Tomography 2013: 736–741.
38. Sardeshpande M v., Kumar G, Aditya T, Ranade V v. Mixing studies in unbaffled stirred tank reactor using electrical resistance tomography. Flow Measurement and Instrumentation 2016. doi:10.1016/j.flowmeasinst.2016.01.003, https://doi.org/10.1016/j.flowmeasinst.2016.01.003.
39. Silva D P, Bránvik T, Dragone G et al. High gravity batch and continuous processes for beer production: Evaluation of fermentation performance and beer quality. Chemical Papers 2008; 62(1): 34–41, https://doi.org/10.2478/S11696-007-0076-6.
40. Štampar S, Sokolič S Š, Karer G et al. Theoretical and fuzzy modelling of a pharmaceutical batch reactor. Mathematical and Computer Modelling 2011; 53(5–6): 637–645, https://doi.org/10.1016/J.MCM.2010.09.016.
41. Szczęsny A, Korzeniewska E. Selection of the method for the earthing resistance measurement. Przeglad Elektrotechniczny 2018. doi:10.15199/48.2018.12.39, https://doi.org/10.15199/48.2018.12.39.
42. Verma D, Agarwal S. Cardiac Arrhythmia Detection from Single-lead ECG using CNN and LSTM assisted by Oversampling. 2018 International Conference on Advances in Computing, Communications and Informatics, ICACCI 2018, Institute of Electrical and Electronics Engineers Inc.: 2018: 14–17, https://doi.org/10.1109/ICACCI.2018.8554541.
43. Wajman R. The concept of 3D ECT system with increased border area sensitivity for crystallization processes diagnosis. Sensor Review 2021; 41(1): 35–45, https://doi.org/10.1108/SR-10-2019-0254.
44. Wanta D, Makowiecka O, Smolik W T et al. Numerical Evaluation of Complex Capacitance Measurement Using Pulse Excitation in Electrical Capacitance Tomography. Electronics (Switzerland) 2022. doi:10.3390/ELECTRONICS11121864, https://doi.org/10.3390/ELECTRONICS11121864.
45. Wanta D, Smolik W T, Kryszyn J et al. Image reconstruction using Z-axis spatio-temporal sampling in 3D electrical capacitance tomography. Measurement Science and Technology 2022. doi:10.1088/1361-6501/AC8220, https://doi.org/10.1088/1361-6501/AC8220.
46. Yan P, Jin H, Tao F F et al. Flow characterization of gas-liquid with different liquid properties in a Y-type microchannel using electrical resistance tomography and volume of fluid model. Journal of the Taiwan Institute of Chemical Engineers 2022; 136: 104390, https://doi.org/10.1016/J.JTICE.2022.104390.
47. Ye Z, Banasiak R, Soleimani M. Planar array 3D electrical capacitance tomography. Insight: Non-Destructive Testing and Condition Monitoring 2013; 55(12): 675–680, https://doi.org/10.1784/INSI.2012.55.12.675.
48. Ziolkowski M, Gratkowski S, Zywica A R. Analytical and numerical models of the magnetoacoustic tomography with magnetic induction. COMPEL - The International Journal for Computation and Mathematics in Electrical and Electronic Engineering 2018. doi:10.1108/COMPEL-12-2016-0530, https://doi.org/10.1108/COMPEL-12-2016-0530.
49. Zywica A R, Ziolkowski M, Gratkowski S. Detailed analytical approach to solve the magnetoacoustic tomography with magnetic induction (MAT-MI) problem for three-layer objects. Energies 2020. doi:10.3390/en13246515, https://doi.org/10.3390/en13246515.